IEEE Access
Multidisciplinary | Rapid Review | Open Access Journal

Received September 25, 2018, accepted October 16, 2018, date of publication October 29, 2018,
date of current version December 18, 2018.

Digital Object Identifier 10.1109/ACCESS.2018.2877932

Preserving-Texture Generative Adversarial Networks for Fast Multi-Weighted MRI

TIAO CHEN, XUEHUA SONG, AND CHANGDA WANG, (Member, IEEE)
School of Computer Science and Communication Engineering, Jiangsu University, Zhenjiang 212200, China

Corresponding author: Changda Wang (changda@ujs.edu.cn)

This work was supported in part by the National Natural Science Foundation of China under Grant 61672269, in part by the National Key Research and Development Program of China under Grant 2017YFC1600804, and in part by the Jiangsu Provincial Science and Technology Project under Grant BA2015161.

ABSTRACT Traditional magnetic resonance imaging (MRI) acquires three contrasts of T_1, T_2, and proton density (PD), but only one contrast can be highlighted in an imaging process, which not only restricts the reference standard for disease but also increases the discomfort and medical expenses of the patients due to requiring two different weighted MRI. In order to solve such a problem, we proposed a method based on deep learning technology to provide two MRI contrasts after one signal acquisition. In this paper, a new model (PTGAN) based on generative adversarial networks is devised to convert T_2-weighted MRI images into PD-weighted MRI images. In addition, we have devised four different network structures as the reference model of PTGAN, by which the different brain dissection MRI images, different noise MRI images, knee cartilage MRI images, and pathological MRI images from different body parts are used to test PTGAN. The research results show that the proposed PTGAN can effectively preserve the structure and texture and improve resolution in the conversion. Moreover, each T_2-weighted MRI conversion takes only about 4 ms and can provide more information for disease diagnosis through different image contrasts.

INDEX TERMS T_2-weighted MRI, PD-weighted MRI, deep learning, generative adversarial networks (GAN), fast conversion, accurate diagnosis, preserve texture.

I. INTRODUCTION

MRI is a multi-functional imaging modality [1]. Since different body structures have different tissue characteristics, the images obtained through the MR scanner can be used to study both the structure and function of the body. The goal of MRI is to construct a digital matrix corresponding to the spatial location. This digital matrix describes the spatial distribution of some characteristics of the sample nucleus [2] such as the density of the nucleus or the relaxation time of the tissue.

Unlike single-density parameter imaging of Computed tomography (CT) [3] examination, the MRI examination has several parameters including T_1 value reflecting T_1 relaxation time, the T_2 value reflecting T_2 relaxation time, and the PD value reflecting the relaxation time of the proton density [4].

The fundamental difference between MRI and other medical imaging methods is that the user can control the method of data acquisition and image reconstruction. The software controls the pulse time, the data acquisition sequence, the intensity and the rate of auxiliary magnetic field to change the contrast, resolution, acquisition of MRI Speed, field of view and artifact effects, etc [5]. The core of these controls is the k-space [2].

Different weighted MRI methods have their own advantages in observing different tissue features. To diagnose diseases, multiple weighted MRI can greatly help medical experts to make a decision. Because of the limitations of medical expenses and the constraints of medical image collection regulations, the fixed contrast display method is applied for different tissues of the body [1]. Medical experts can only roughly make a judgment according to the single-weighted MRI. For the more complicated and serious diseases, further checkings are required through different weighted MRI, which also increases patients discomfort and medical costs during the secondary acquisition.

In recent years, deep learning has developed rapidly in many different fields, and has shown amazing advantages [6]. The artificial neural network model learns the statistical rules from a large number of training samples through the backpropagation algorithm [7] and forms a more abstract

high-level representation by combining the lower-level features to discover the distributed features representing the data [8]. This kind of statistical rules-based deep learning method is superior to the past system based artificial rules [9]. Some excellent deep neural network models are then widely used, such as convolutional neural networks (CNN) [10] for images processing and recurrent neural networks [11] for speech processing.

We use the improved Generative Adversarial Networks (GAN) [12] to creatively convert T_2-weighted MRI images into PD-weighted MRI images, which provides more references for disease diagnosing. At the same time, for the problem of image segmentation [13], [14], detection [15], [16], classification [17]–[19] and registration [20], [21] caused by medical image training data, we devised an efficient method to preprocess the training data. The follows are our specific contributions:

- We proposed a U-Net architecture [22], [23], with seven skip connections for the generator model, where the L2 loss [24] and normalized mean square error (NMSE) consists of the generator loss of the model.
- We proposed to append k-space frequency domain loss, including frequency edge loss and frequency center loss, to the generator loss, by which to obtain high organizational similarity and resolution after image conversion.
- We performed a large number of comparative experiments to evaluate PTGAN, which illustrate both the effective and efficiency of our proposed method.

II. METHOD

The key to traditional MRI is the radio frequency (RF) pulse sequence. Different RF pulse sequences highlight the contrast of different tissue signals. Different pulse sequences are distinguished by sequence parameters such as RF pulse duration and interval time. Under the support of traditional MRI principles, we use the improved deep GAN to obtain multi-weighted MRI images after one signal acquisition.

A. TRADITIONAL MRI METHOD

The existing MRI method place patients in strong magnetic field and uses radio RF pulse with the same frequency for proton precession [1], [25]. The protons resonated after absorbing energy. The radio frequency pulse with the same precession frequency can be calculated by the Larmor equation [26]:

$$\omega_0 = \delta \cdot B_0 \tag{1}$$

where ω_0 denotes the precession frequency; δ denotes the gyromagnetic ratio. The gyromagnetic ratio of different materials is different. B_0 denotes the magnetic field strength in the RF pulse. Its frequency increases as the field strength increases.

Under the action of a strong magnetic field, the protons are arranged in an order and rotate in a cone along the axis of rotation, and the longitudinal magnetization is then reduced to produce transverse magnetization [27].

The RF pulse sequence determines the contrast of the tissue signal. For long repetition time (TR) of pulses (>1500ms), the difference of tissue signal depends on PD contrast instead of T_1 contrast. When echo time (TE) is extremely short (<20ms), the difference among T_2 signal intensities is small. When TE is great than 50ms and less than 200ms, the difference among signal intensities depends on T_2 contrast. For spin echo pulse sequences, T_1-weighted MRI, T_2-weighted MRI, and PD-weighted MRI can be obtained through different TR and TE [28], [29].

In the case of a long TR and a long TE, T_1 contrast is weakened and T_2 contrast is prominent. In the case of short TR and short TE, T_1 and T_2 contrasts are weaken. In the case of long TR and short TE, the longitudinal magnetization of the two different tissues has completely recovered after TR time, which leads to the inability to highlight T_1 contrast [26], [30]; in the short TE, the T_2 contrast of different tissues cannot be highlighted, and the comparison of different tissue signals only rely on the difference of PD [31].

Fig.1 shows T_2-weighted MRI and PD-weighted MRI principles. In T_2-weighted pulse sequence, the longitudinal magnetization vector in the scan period of the long TR has been fully relaxed by the T_1 time constant, and the long TE further excludes T_1 effect in the signal. In PD-weighted pulse sequence, the long TR allows the longitudinal magnetization vector of the tissue to fully relax before the next excitation, which reduces the effect of T_1 on the signal. The short TE mainly reduces the effect of T_2 on MRI, which makes the contrast of MRI only related to the PD [30], [31]. Different sequence parameters highlight some contrasts in the image and greatly reduce the effects of other contrasts [32], [33].

Transverse magnetization and longitudinal magnetization synthesize the total magnetic vector, and MRI scanner senses the current as well as receives the signal from body. The strongest signal M after 90° pulse is:

$$M = M_0(1 - e^{-TR/T1})e^{-TE/T2} \tag{2}$$

in which $T1$ is the time required for the recovery of the longitudinal magnetization to 63% of the original magnetic vector and $T2$ is the time required for the transverse magnetization to decrease to 37% of the original magnetic vector [4]. No matter which kind of weighted MRI, there will always be three contrasts: PD, T_1 and T_2. In particular, regardless of the TR and TE values, the signal received by NMR instrument is always affected by the proton density [28], [29], [31]. A certain degree of relaxation has occurred before the available measurement signals appearing, which provides the possibility of that convert T_2-weighted images to PD-weighted images.

B. GENERATIVE ADVERSARIAL NETWORKS

1) GENERAL GAN

Generative Adversarial Networks provides a way to learn deep representations [8] without extensively labeling training data. The GAN includes a generator model G and

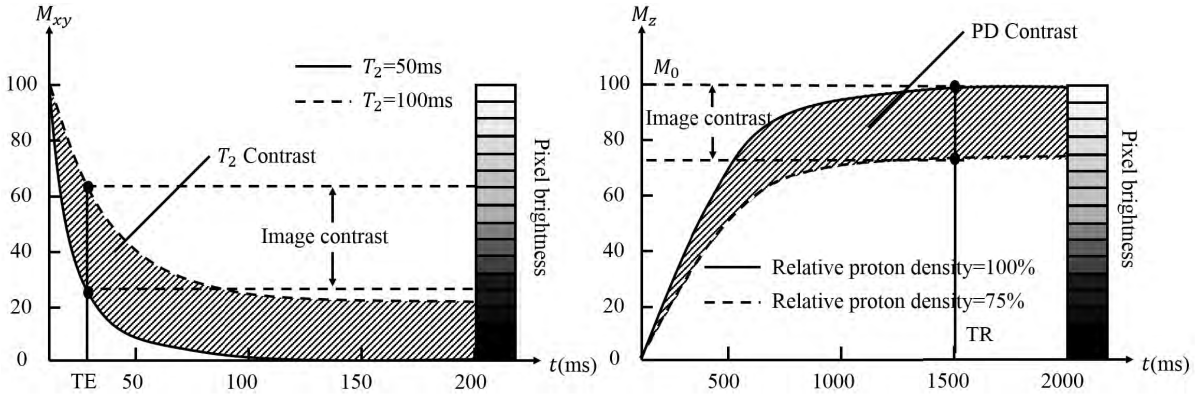

FIGURE 1. T_2-weighted and PD-weighted MRI principles.

a discriminator model D, which are completely independent of the two models. G captures the data distribution and D estimates the probability of the sample from real data. The two networks are updated by a back propagation algorithm to perform competitive learning for training purposes [7], [12].

The generator model and the discriminator model are usually composed of a multi-layer network containing convolution or fully connected layers. The generator G learns the distribution P_g of the real data x and uses fake data $G(z)$ to map the priori variable $P_z(z)$ of the input noise. The discriminator model D outputs a single scalar. The training of D and G is a minimax game problem of the value function $K(G, D)$:

$$\max_D K(D,G) = E_{x\sim P_{data}(x)}[\log D(x)] + E_{z\sim P_z(z)}[\log(1-D(G(z)))] \quad (3)$$

$$\min_G K(D,G) = E_{z\sim P_z(z)}[\log(1-D(G(z)))] \quad (4)$$

D maximizes the assignment of the correct label to the real data and G-generated the samples through training [12]. After optimization by the stochastic gradient ascent algorithm [34], $D(x)$ is continuously improved and $D(G(z))$ is then gradually reduced.

At the same time, G minimizes the $log(1 - D(G(z)))$ by stochastic gradient descent algorithm [35], [36], which maximizes the probability used by the G-generated sample to judge the real data.

$$D^*_G(x) = \frac{P_{data}(x)}{P_{data}(x)+P_g(x)} \quad (5)$$

In equation (5), the generator model and the discriminator model eventually reach a balance optimal state as $P_g = P_{data}$ [12] during the adversarial training process. The generator model captures the data manifold of P_{data} and maps the generated data distribution to the real data, which indicates that the GAN network achieves the best training effect.

2) LEAST SQUARES GAN

General GAN use the KL divergence [37] to measure the difference between P_g and P_{data}. The optimization of the general GAN loss function is equivalent to minimizing the Jensen-Shannon divergence [38]. And the least-squares GAN [40] redefines the loss function as follows:

$$\min_D K(D,G) = \frac{1}{2}E_{x\sim P_{data}(x)}[D(x)-a]^2 + \frac{1}{2}E_{z\sim P_z(z)}[D(G(z))-b]^2 \quad (6)$$

$$\min_G K(D,G) = \frac{1}{2}E_{x\sim P_{data}(x)}[D(x)-c]^2 + \frac{1}{2}E_{z\sim P_z(z)}[D(G(z))-c]^2 \quad (7)$$

In $\min_G k(D, G)$ of equation (7), there is one more $E_{x\sim P_{data}(x)}[D(x)-c]^2$ as a constant independent of G network than the original loss function [12]. The constants a and b respectively represent the mark of real images and generated images; the role of c is to maximize $D(G(z))$ which determines the probability that $G(z)$ is the real data. After fixing G, the optimization formula of discriminant model D is:

$$D^*(x) = \frac{bP_{data}(x)+aP_g(x)}{P_{data}(x)+P_g(x)} \quad (8)$$

The optimization objective function of Jensen-Shannon divergence based on the least-squares loss is equivalent to minimizing the Pearson χ^2-divergence [39] between $P_{data} + P_g$ and $2P_g$ under the constraints $a - c = 1$ and $a - b = 2$.

$$2S(G) = \chi^2_{pearson}(P_{data}+P_g \| 2P_g) \quad (9)$$

According to the constraints for a, b, c, the adversarial loss under the least-squares loss function is:

$$\min_D K(D,G) = \frac{1}{2}E_{x\sim P_{data}(x)}[D(x)-1]^2 + E_{z\sim P_z(z)}[D(G(z))]^2 \quad (10)$$

$$\min_G K(D,G) = \frac{1}{2}E_{z\sim P_z(z)}[D(G(z))-1]^2 \quad (11)$$

The loss function in equation (10) and (11) is a basic adversarial loss for PTGAN that replaces the sigmoid cross-entropy loss function in the conventional GAN. It has better conversion effect and more stable training process than that of the conventional GAN.

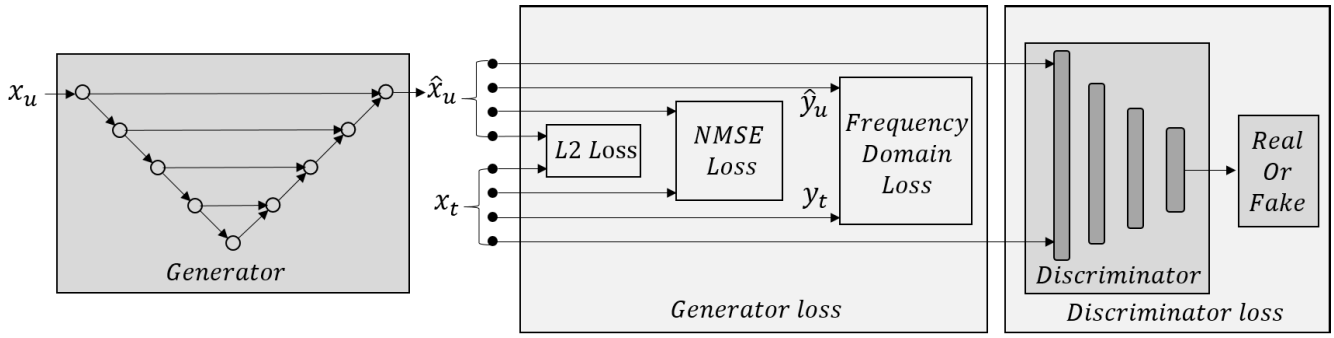

FIGURE 2. Schema for our proposed GAN-based preserving-texture for fast multi-weighted MRI(PTGAN).

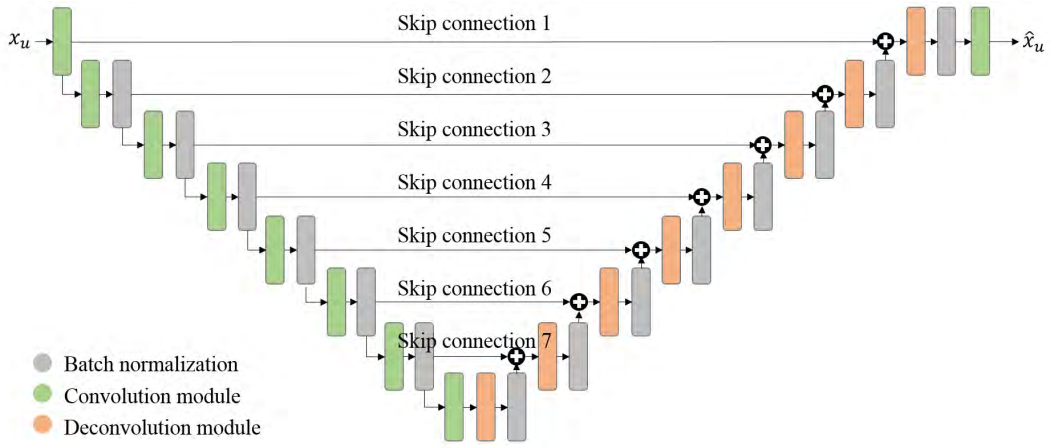

FIGURE 3. Network structure of U-Net as generator.

C. PROPOSED METHOD

1) PROPOSED ARCHITECTURE

In the proposed PTGAN, U-Net with well performance in medical image processing is used as a generation model, which can effectively preserve the organization structure of T_2-weighted images during the conversion. Fig. 2 shows the overall structure of PTGAN model.

The network structure of U-Net as the generation model in PTGAN is shown in Fig. 3. Generator G contains 8 convolution modules and 8 deconvolution modules [10]. The symmetry encoder and decoder perform additional operation as the output of the decoder, which preserves the structural texture details of MRI images as much as possible. Discriminator D uses a classical convolutional neural network with 10 convolutional modules.

2) GENERATOR LOSS

In order to obtain better image conversion quality, we add the normalized mean square error loss, L2 loss and frequency loss to the loss function of the generator G based on the basic adversarial loss of PTGAN. The normalized mean square loss can be expressed as:

$$\min_G L_{nmse}(G) = \frac{\|x_t - \hat{x}_u\|_2^2}{\|x_t\|_2^2} \tag{12}$$

where x_t is the real PD-weighted MRI images acquired by the pulse sequence, and $\hat{x}_u$ is the PD-weighted images converted by T_2-weighted images.

In order to prevent over-fitting [41], [42] during the training, L2 regularization is performed in the generation loss, which is the penalty [41] of the sum of L2 norms [43] with parameters:

$$\min_G L_{l2}(G) = \frac{\theta}{2n}\sum_w w^2 \tag{13}$$

$$C = C_0 + L_{l2} \tag{14}$$

where w is the weight in neural network; C_0 represents the original cost function; and n is the number of samples; θ is a regular term coefficient that weighs the proportion of the regular term and C_0.

In L2 regularization, the parameters in the neural network are updated by:

$$w := w + \mu\frac{\partial C_0}{\partial w} + \phi\frac{\theta}{n}w \tag{15}$$

where $\mu < 0$ and $\phi < 0$ in the gradient descent algorithm and $\mu > 0$ and $\phi > 0$ in the gradient ascent algorithm.

In order to solve low image quality after conversion, we calculate the loss function by reflecting the characteristics of the spatial frequency. In the k-space of MRI, the edge

Algorithm 1 Proposed Preserving-Texture GAN Algorithm

Initialize all parameters of the generator G and discriminator D
for number of epoch **do**
  for k steps **do**
    Input: minibatch of m T_2-weighted MRI images $z^{(1)}, \ldots, z^{(m)}$ from $P_z(z)$ and minibatch of m PD-weighted MRI images $x^{(1)}, \ldots, x^{(m)}$ from $P_{data}(x)$
    Output: $G(z)$, $D(G(z))$, $D(x)$
    Updade the discriminator D by Adam-based stochastic gradient descent:
    $\nabla_{\theta_g} \frac{1}{m} \sum_{n=1}^{m} [(D(x) - 1)^2 + (D(G(z)))^2]$
    Updade the generator G by Adam-based stochastic gradient descent:
    $\nabla_{\theta_d} \frac{1}{m} \sum_{n=1}^{m} (\alpha L_{nmse} + \beta L_{l2} + \gamma L_{fft} + \lambda L_{ls})$
  end for
  evaluation for validation data based on early stop strategy strategy
end for

portion determines the overall structure of the image, while the central portion determines the image resolution [44].

$$\min_G L_{fft}(G) = \frac{1}{2} \left\| y_t - \hat{y}_u \right\|_2^2 \tag{16}$$

where y_t and $\hat{y}_u$ are the data of k-space with respect to x_t and $\hat{x}_u$. The G-generated MRI images and the real MRI images are mapped to k-space by Fourier transform. The high resolution and structural boundary of the MRI images are preserved by reducing the difference between y_t and $\hat{y}_u$ at low and high frequencies.

In this paper, the least-squares loss function replaces the sigmoid cross-entropy loss function, the loss function of the generator model in the basic adversarial loss can be expressed as:

$$\min_G L_{ls}(G) = \frac{1}{2} \left\| D(G(x_u)) - 1 \right\|_2^2 \tag{17}$$

Therefore the total loss function can be expressed as:

$$L_{total} = \alpha L_{nmse} + \beta L_{l2} + \gamma L_{fft} + \lambda L_{ls} \tag{18}$$

in which α, β, γ, and λ are hyperparameters for each part of the loss. Model training and optimization are included in Algorithm 1.

3) EVALUATION METHOD

In order to fully test the conversion effect of PTGAN model, we first perform conversion of T_2-weighted MRI images in DICOM format from three different brain sections including horizontal plane, sagittal plane, and coronal plane. Secondly, we also convert T_2-weighted MRI images at the knee where PD contrast is often used. Finally, T_2-weighted MRI images of tumors from 7 different parts of the body and T_2-weighted MRI images containing 1%, 3%, 5%, and 7% noise rate were tested. The converted PD-weighted MRI images are evaluated by three evaluation indicators: NMSE, PSNR, and SSIM.

a: MODEL COMPARISON

We devised four different network models as the references in the paper: (1) Convolutional Neural Network (**CNN**): Including 8 convolution modules and 8 deconvolution modules; (2) **U-Net** model: Compared to CNN model, U-Net uses skip connections to attach symmetrical convolution module and deconvolution module; (3) CNN-based GAN (**CNN-GAN**): CNN as the generation model of GAN; (4) **U-Net_refine-GAN** [45]: Adding a skip connection in PTGAN. In the above four cases, the test results were compared by which to measure the conversion quality of each case.

b: LOSS FUNCTION COMPARISON

In our work, the conversion effects of PTGAN were tested separately in the cases of different loss functions: (1) only the least-squares loss (**LS**) in the basic adversarial loss; (2) the least-squares loss and the L2 loss (**LSL**); (3) Least-squares loss, L2 loss and normalized mean square error loss (**LSLN**); (4) Contains least-squares loss, L2 loss, normalized mean square error loss and frequency loss (**LSLNF**). In the above four cases, the test results were compared by which to measure the conversion quality of each case.

III. EXPERIMENTS

A. EXPERIMENT SETTINGS

1) DATASET

The training data and test data used in the paper are from the IXI database (http://brain-development.org/ixi-dataset/). The raw data samples are 3D brain MRI images in NIFTI format acquired at a magnetic field strength of 1.5T. We extracted 47,252 2D training images and 17,848 2D evaluation images from 499 3D brain images. At the same time, 10,230 2D test images were extracted from 78 3D brain MRI images, and 50 2D images were randomly selected for comparison. We also used seven different tissue tumor images (http://www.cancerimagingarchive.net/) for testing. The size of the 2D MRI image is 256×256. The pixel values of T_2-weighted MRI images and PD-weighted MRI image acquired by a pulse sequence are normalized within [−1, 1], which ensures that each part of the entire image can be trained to the same extent. In addition, the training data was mixed with 3%, 5%, and 7% of Gaussian white noise, which increased data diversity and improves the anti-interference ability of the model.

2) IMPLEMENTATION

The implementation of PTGAN model relies on TensorLayer [46] framework, an advanced deep learning library that provides an easy-to-use API based on TensorFlow. The hardware configuration of the implementation includes Intel(R)

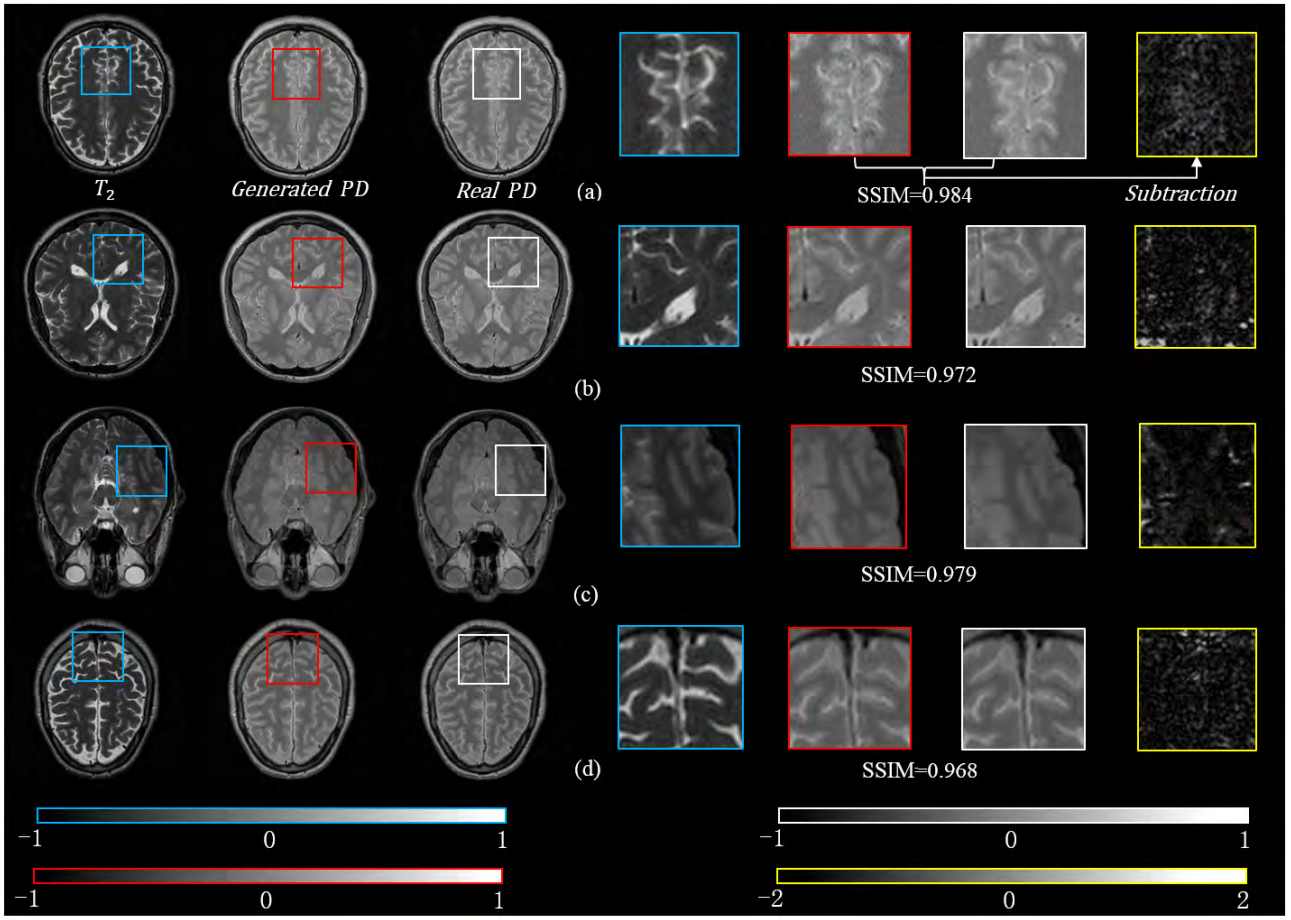

FIGURE 4. Conversion result of PTGAN model under LSLNF loss. Blue box represents the zoomed-in Region of Interest (ROI) (50×) of the T_2-weighted MRI images. Red box indicates zoomed-in ROI (50×) corresponding to the PD-weighted MRI images after the PTGAN conversion. White box indicates zoomed-in ROI (50×) corresponding to the PD-weighted MRI image acquired by a pulse sequence. Yellow box indicates the difference between the generated images and PD-weighted MRI image acquired by a pulse sequence. Color bars are shown at the bottom.

Xeon(R) CPU E5-2630 v4 (×4), 128GB RAM and Tesla P100-PCIE-16GB GPU (×2).

3) TRAINING SETTING

After comparing the simulation results under different parameter settings, the loss function in the experiment was set by the hyperparameters of $\alpha = 15$, $\beta = 1$, $\gamma = 1$, and $\lambda = 1$. The PTGAN was initialized at a learning rate of 0.1E-3 and a batch size of 50. In model optimization, the PTGAN use a standard Adam optimization algorithm [47] with momentum of 0.9. The generator G and the discriminator D contain a batch normalization module [48] before the input of each layer, which solves the problem that is difficult to train due to the increase in the number of neural network layers.

B. RESULTS

Fig. 4 is the conversion results of PTGAN model under LSLNF loss. The physical condition of a patient is the basis for acquiring MRI images. Therefore, it is necessary to ensure that the image texture cannot be changed during the conversion, which is the rule we must be followed. In Fig. 4, we can get overall structural similarity between the generated images and the real PD-weighted MRI images. Furthermore, we can continue observing the similarity of texture details from the zoomed-in ROI (50×).

We selected 50 differently shaped brain horizontal plane conversion images to compare with ground truth (GT). The average SSIM reached 0.971, while the converted images had an average PSNR of 32.944 dB. Evaluation indicator such as SSIM or PSNR is a digital only representation, so we also provided MRI images and zoomed-in ROI in the paper. In order to show the changes in detail, we enlarged the ROI by 50 times and used GT as the quality reference for the generated images in Fig. 4. As a result, different highlights can be observed by the visual comparison between blue box and red box in the zoomed-in ROI. It can be seen from Fig. 4 that the T_2-weighted MRI images have obvious tissue structure with the poor detail effects. Although contrast of the converted PD-weighted MRI images is relatively low, the edge of the organizational structure is clear and the details are contrasted, which is conducive to the accuracy of disease diagnosis.

TABLE 1. Quality evaluation of brain MRI images conversion under different noise.

Noise Ratio	NMSE	SSIM	PSNR
0%	0.177±0.031	0.971±0.014	32.953±3.622
1%	0.182±0.033	0.970±0.012	32.486±3.263
3%	0.187±0.032	0.969±0.015	32.115±3.623
5%	0.189±0.036	0.961±0.013	30.708±3.539
7%	0.195±0.031	0.959±0.014	30.631±3.867
9%	0.211±0.056	0.949±0.019	28.895±4.416

In addition to evaluation indicator, MRI images, zoomed-in ROI, we also in Fig. 4 provided the image difference between red boxes and white boxes by the yellow boxes. The smaller the pixel value in the yellow boxes is, the smaller the differences are. It can be observed from the yellow boxes in Fig. 4 that there is no obvious texture structure distribution, which shows that the difference in texture and structure between the generated images and GT is extremely small. It also verifies that the generated images retaining the texture and structure during the conversion.

In this study, we test T_2-weighted MRI images under five different degrees of Gaussian noise. It can be seen from Fig. 5 that when the Gaussian noise ratio is less than 5%, the black portion in the yellow box is relatively large, which indicates that the conversion difference is relatively smaller. In Table 1, the average PSNR of the converted images is great than 32 dB when the Gaussian noise is less than 5%. However, when the Gaussian noise is great than 5%, the PSNR of the converted PD images is great than 31 dB. As the noise increases, the quality of the conversion decreases. Although the T_2-weighted images with 9% Gaussian noise is not included in the training data, a better conversion effect with an average SSIM as 0.949 can still be obtained.

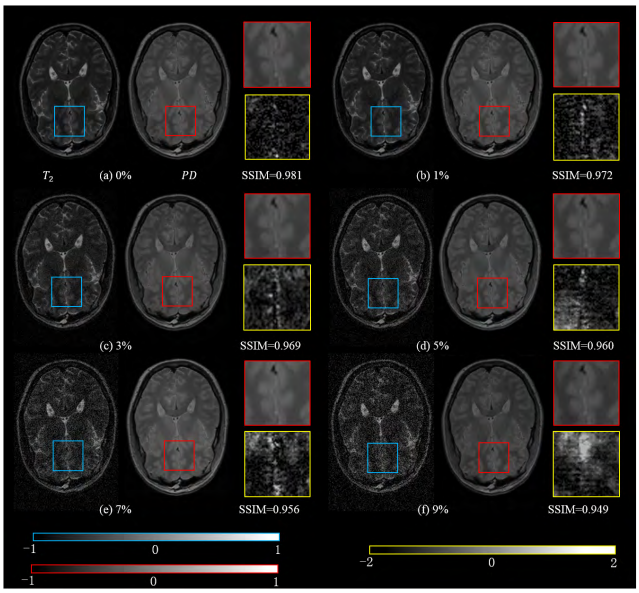

FIGURE 5. Conversion results under different noises ratio, where blue box represents the zoomed-in ROI of the T_2-weighted MRI images; red box indicates zoomed-in ROI (50×) corresponding to the PD-weighted MRI images after the PTGAN conversion; yellow box indicates the difference between the generated images and GT. Color bars are shown at the bottom.

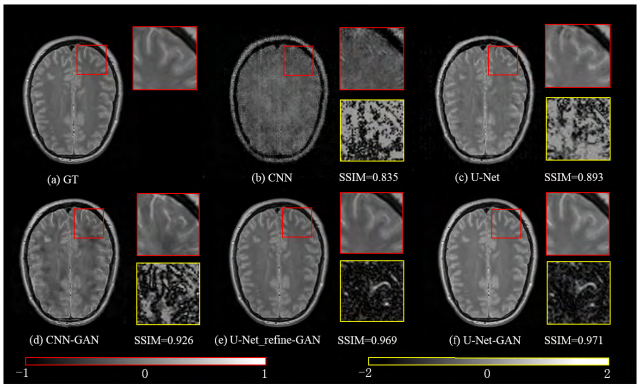

FIGURE 6. Converted PD-weighted MRI images under five different network models. (a) is ground truth (GT) that a PD-weighted MRI image acquired by a pulse sequence. Red box indicates zoomed-in ROI (50×) corresponding to the PD-weighted MRI images. The image conversion results with CNN (b), U-Net (c), CNN-GAN (d), U-Net_refine-GAN (e), PTGAN (f) under LSLNF loss were presented after five different networks conversion, the yellow box indicates the difference between the generated images and GT. Color bars are shown at the bottom.

IV. DISCUSSION

In order to fully test the conversion effect of PTGAN model, we converted T_2-weighted MRI images from different parts of the body. We also designed five different network models for comparisons. In addition, the conversion effects of PTGAN were tested separately in the case of different loss functions.

A. MODEL COMPARISON

There are no other methods for multiple-weighted MRI, in order to evaluate PTGAN, we additionally applied four deep learning networks to multiple-weighted MRI. Based on the principle of fair comparison, CNN or U-Net in different models have the same network depth, and the discriminators in different GAN also have the same network depth. All models are in the same training data, test data and experimental environment. Due to the requirements of the model structure, CNN and U-Net use the L_{nmse}, L_{l2} and L_{fft}, and the remaining GAN models use the LSLNF loss function.

It can be seen from Fig. 6 (b) that the image after conversion is blurred, which can only identify the outline of the horizontal plane of the brain and cannot observe the structure of the brain. In summary, there are more image noise and poorer image quality in Fig. 6 (b). Compared to Fig. 6 (b), the basic brain structure of section can be observed in Fig. 6 (c) and the black area in the yellow box increases, which indicates that the difference between the generated image and GT has been reduced. However, the image resolution is not high and the details are blurred, which is not conducive to observing the texture in Fig. 6 (c). At the same time, irregular black blocks appear at horizontal anatomical surface in Fig. 6 (c), which is easy to mislead the observation of the condition. The image in Fig. 6 (d) has a higher resolution and a clear

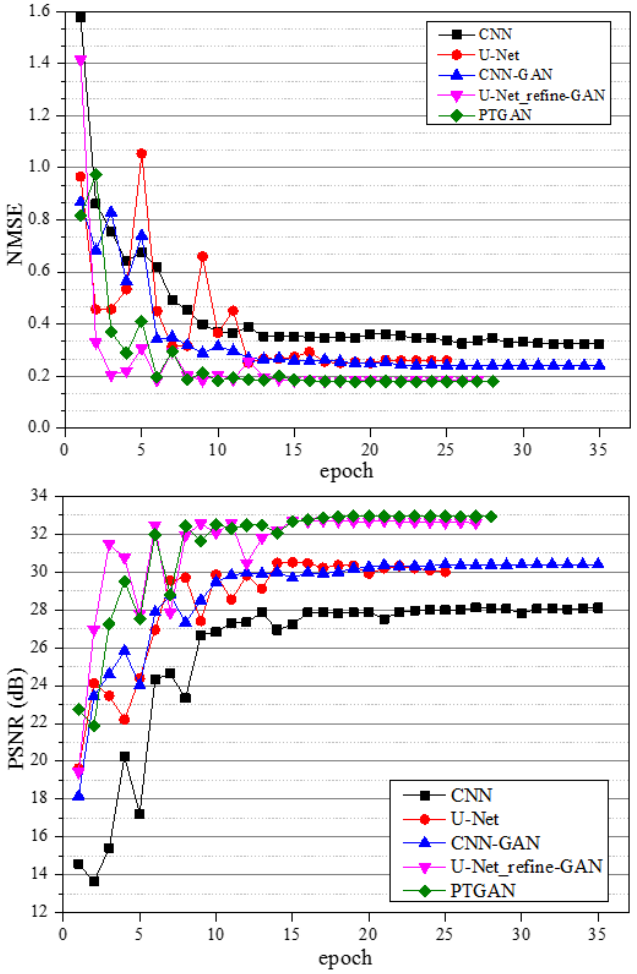

FIGURE 7. Changes of NMSE and PSNR in different models with LSLNF loss under training.

structure, but the number of black irregular blocks increases, which adversely affects the diagnosis. In Fig. 6 (e), the black irregular block disappears and the image quality is increased accordingly. The SSIM in Fig. 6 (f) is 0.971, where the image texture is prominent and the structure is clear. As a result, It is of great help to brain structure research and disease diagnosis.

Fig. 7 shows the changes in NMSE and PSNR of different models with the training. As the NMSE decreases, the PSNR continues to increase, which proves that the quality of the conversion is also improving. It can be seen that GAN has obvious advantages over applying CNN alone. U-Net also exhibits similar conversion effects to CNN-GAN by virtue of its advantages in medical image processing. Since U-Net_refine-GAN adds the input image to the output image directly through a skip connection in the last layer of the generator model, the output PD-weighted MRI containing more T_2-weighted components. Therefore, the effect of U-Net_refine-GAN is not as good as that of PTGAN.

B. LOSS FUNCTION COMPARISON

The selection of the loss function is extremely important for the conversion quality and training process of PTGAN.

TABLE 2. Quality evaluation of brain MRI images conversion under different losses.

Method	NMSE	SSIM	PSNR	Test Time CPU(ms)/GPU(ms)
LS	0.195±0.042	0.960±0.016	31.221±3.856	48.4±0.3/4.0±0.3
LSL	0.190±0.043	0.964±0.015	31.399±3.510	48.4±0.3/4.0±0.3
LSLN	0.181±0.035	0.969±0.015	32.405±3.602	48.4±0.3/4.0±0.3
LSLNF	0.177±0.031	0.971±0.014	32.953±3.622	48.4±0.3/4.0±0.3

Since the sigmoid function in the cross-entropy loss is easy to reach the saturation state, the GAN training is unstable, and the least-squares function is saturated at only one point. But this is only theoretically proven, and still requires a true comparison of results. Therefore, we trained the cross-entropy loss and least squares loss models under the same experimental conditions and compared them under the same evaluation criteria. In addition, loss functions correspond to the properties of MRI images and will have a significant impact on the resolution and detail of the converted images during training. We used the incremental loss function to train and test separately under the same experimental conditions and evaluation criteria, which can more intuitively observe the impact of the loss function on image conversion.

It can be seen from Fig. 8 that the least-squares loss is superior to the sigmoid cross-entropy loss in both the NMSE and PSNR evaluation indexes and converges smoothly. The sigmoid cross-entropy loss with large convergence fluctuations caused the training to end prematurely at 13th epoch, which is not conducive to finding the global optimal solution. Although the NMSE of the least-squares loss function is large at the beginning of training, the fluctuation begin to gradual after 5 epochs, and finally the training stops at 28th epoch. The convergence of the whole training process is less fluctuating and the training is stable.

In Table 2, as the type of loss function increases, the NMSE continues to decline and the conversion quality is also improved to varying degrees. At the same time, while the standard deviation of the NMSE continues decreasing, the data fluctuation range is reduced accordingly. Therefore, the PTGAN model tends to be stable. When only LS loss was used, the average SSIM of the converted images reached an observable level of 0.960. As the increase of loss function, the conversion accuracy of PTGAN have also been improved. The texture details of the structure were preserved while maintaining the transformation of the organizational structure. Compared to the LS loss function, the PSNR of the converted images under LSLNF was increased by 1.732dB when NMSE was reduced by 0.018. And the conversion time under LSLNF is extremely short (about 52ms in independent CPU processing or only 4ms in dedicated GPU computing).

C. LOSS WEIGHT COMPARISON

Different loss functions contribute differently to the generated image, and the proportion of the loss function determines the speed of training. L_{nmse} determines the quality of the

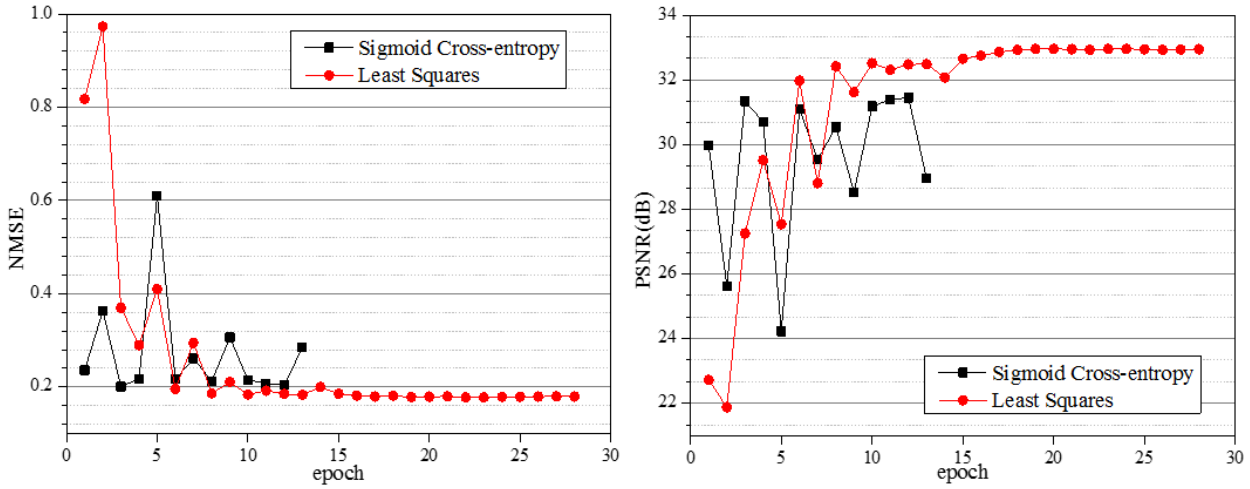

FIGURE 8. Comparison of sigmoid cross-entropy loss and least square loss on PSNR and NMSE under training.

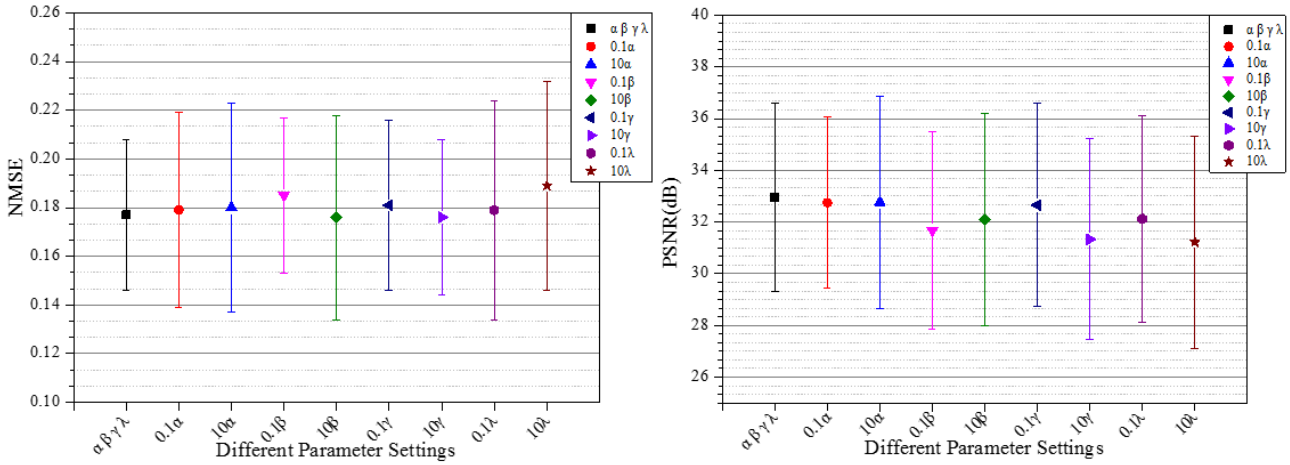

FIGURE 9. Comparison of NMSE and PSNR with different hyperparameters under LSLNF loss.

converted images, a appropriate proportion of L_{nmse} is beneficial to the fast convergence of PTGAN. We compared nine weights for the hyperparameters of the total generated loss function under PTGAN model. First, $\alpha = 15$, $\beta = 1$, $\gamma = 1$, and $\lambda = 1$ are taken as initial values. When the variable-controlling approach were used to keep the other three variables fixed, the four parameters of α, β, γ, and λ were changed by 10 times and 0.1 times of initial values, respectively. In Fig. 9, although the values of the nine different values of α, β, γ, and λ do not fluctuate significantly under three different evaluation criteria, the evaluation index with NMSE, SSIM and PSNR at $\alpha = 15$, $\beta = 1$, $\gamma = 1$, and $\lambda = 1$ are better than the other 8 values.

D. ROBUSTNESS OF PTGAN

Robustness is an important indicator of model stability and practical application. Robustness testing of PTGAN needs to follow the principle of increasing difficulty so that the conversion results of non-training data can be better observed. Since our training data are all from MRI images of the brain, we first tested different sections images and pathological MRI images from brain. Secondly, in order to verify that PTGAN does not learn the shape characteristics of the image, we need to test the MRI image of other parts. Considering the application scope of PTGAN, and T_2-weighted MRI is most commonly used on soft tissue, this is a good validation option. Finally, although we initially tested the tumors in the brain, in order to rule out the interference of brain image features contained in the training, we chose another conventional tumor images in six different parts for testing. T_2-weighted images from the coronal plane, sagittal plane, and horizontal plane of the brain were transformed to test the robustness of the PTGAN model. It can be seen from Fig. 10 that the conversion effect of the coronal plane and horizontal plane is better, and the SSIM reached medical observation levels of 0.956 and 0.975, respectively.

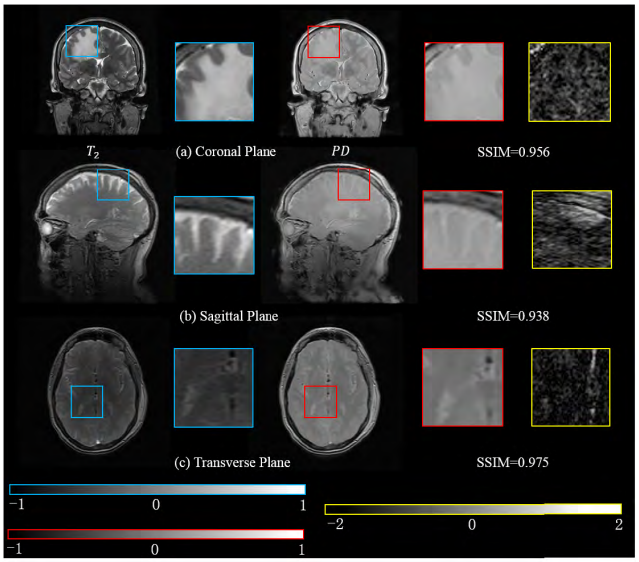

FIGURE 10. Conversion of three different brain anatomical planes under PTGAN. Blue box represents the zoomed-in ROI of the input T_2-weighted MRI images. Red box indicates zoomed-in ROI (50×) corresponding to the PD-weighted MRI images after the PTGAN conversion. Yellow box indicates the difference between the generated images and GT. Color bars are shown at the bottom.

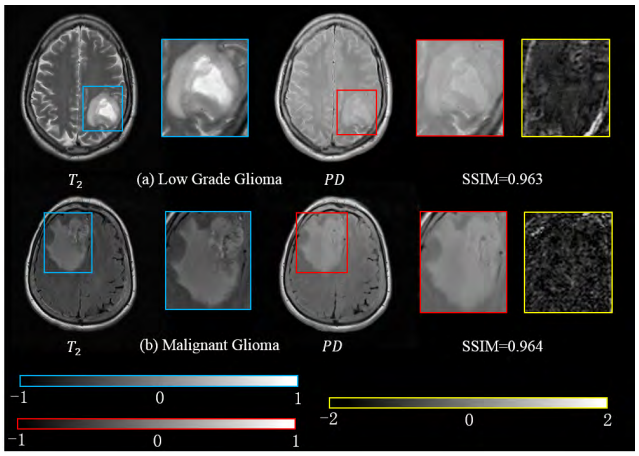

FIGURE 11. Conversion of different grades of glioma in the brain under PTGAN. Blue box represents the zoomed-in ROI of the input T_2-weighted MRI images. Red box indicates zoomed-in ROI (50×) corresponding to the PD-weighted MRI images after the PTGAN conversion. Yellow box indicates the difference between the generated images and GT. Color bars are shown at the bottom.

Although the converted sagittal image shows motion artifacts at the neck, the brain region is structurally intact and the tissue is clearly visible, which does not have a decision-making impact on the diagnosis for brain problems.

In Fig. 10 (b), it also can be observed from the ROI magnified that the texture distribution of the difference image and the texture distribution of the converted image are in the same position, which also shows that the texture distribution of the converted image has not changed. In different contrast experiments, the quality of the converted images is different due to the difference of the models and the input images,

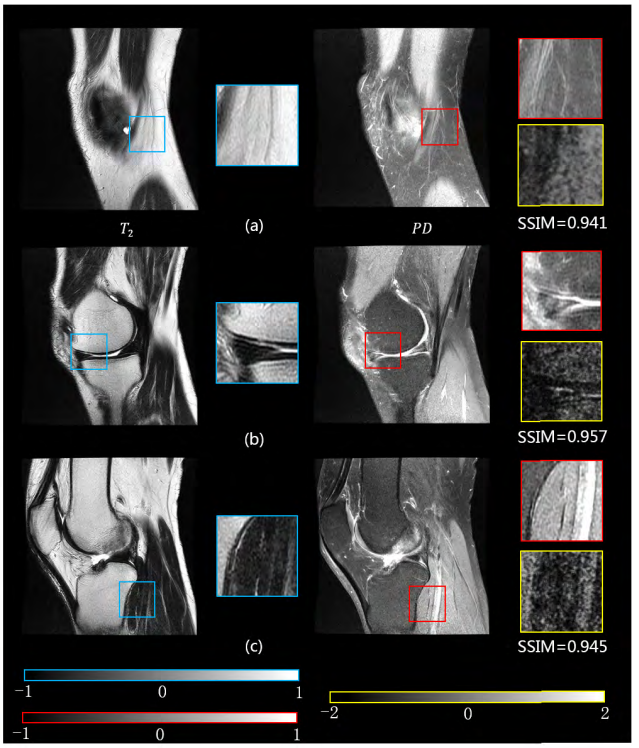

FIGURE 12. Conversion results at knee cartilage. Blue box represents the zoomed-in ROI of the input T_2-weighted MRI images. Red box indicates zoomed-in ROI (50×) corresponding to the PD-weighted MRI images after the PTGAN conversion. Yellow box indicates the difference between the generated images and GT. Color bars are shown at the bottom.

so the image after subtracting the converted image from the real image leave different texture distribution at the same position.

Fig. 11 (a) shows the results of PTGAN conversion of Low Grade Gliomaand and Fig. 11 (b) shows the results of PTGAN conversion of Glioblastoma. In the absence of brain tumor images for training, SSIM of different scales of glioma after transformation is great than 0.96. The glioma edge details in the converted MRI images are highlighted to facilitate observation of tumor lesions.

PD-weighted MRI is often used at the site of the knee cartilage. Fig. 12 shows the conversion results of T_2-weighted MRI images on three different observation surfaces at the knee. The converted image is clear, and the higher quality details can be seen in the zoomed-in ROI.

We selected six different tissue tumor images for testing, including lung adenocarcinoma, liver hepatocellular carcinoma, prostatic cancer, mammary cancer, renal carcinoma and endometrial cancer. It can be observed from Fig. 13 that the conversion results for lung adenocarcinoma and prostatic cancer are relatively good. In Fig. 13 (b), comparing the 50× ROI of the tumor at the same site before and after the conversion, it can be found that the image is changed from the original strong contrast display mode to the prominent detail display, and the surface contour and the wrinkle direction of the tumor can be observed in the red box. The hepatic hepatocellular carcinoma image after conversion in Fig. 13 (a)

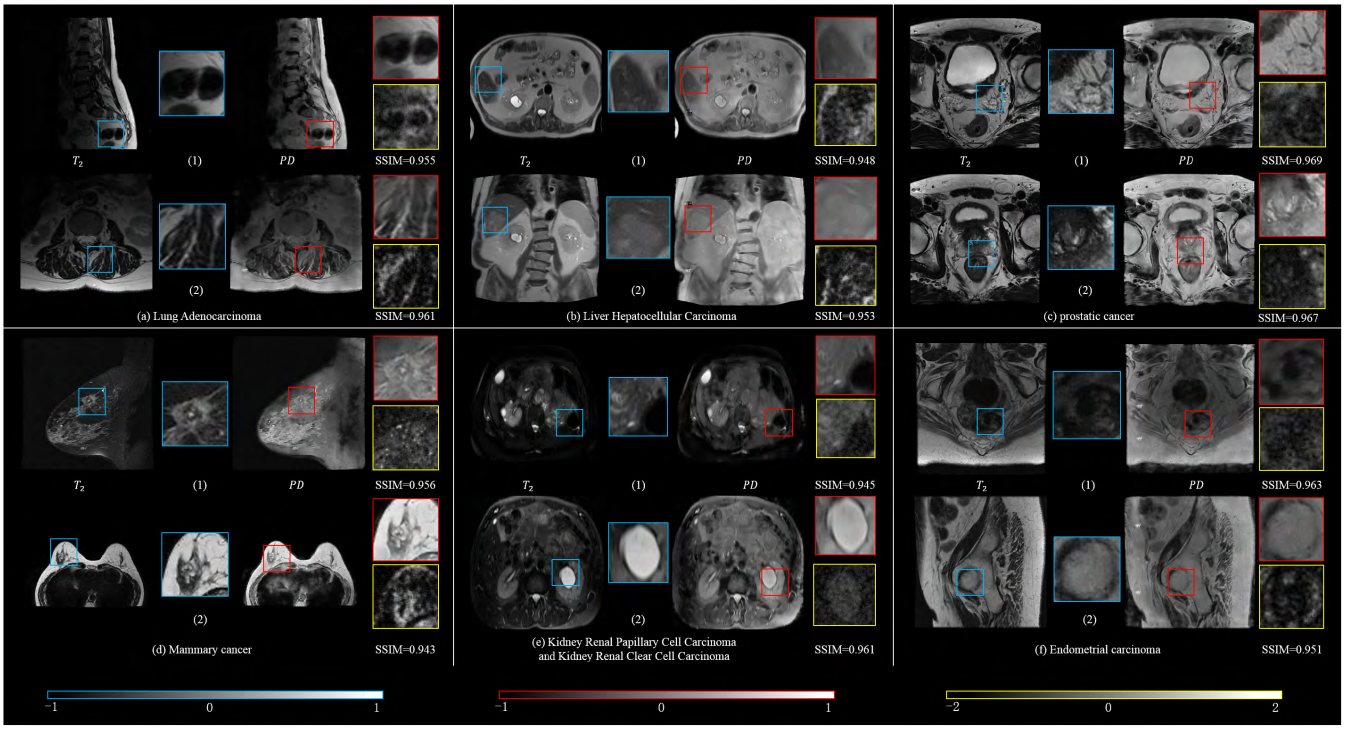

FIGURE 13. Six different tissue tumor images for testing. Blue box represents the zoomed-in ROI of the input T_2-weighted MRI images. Red box indicates zoomed-in ROI (50×) corresponding to the PD-weighted MRI images after the PTGAN conversion. Yellow box indicates the difference between the generated images and GT. Color bars are shown at the bottom.

has a relatively low contrast and a prominent edge shape. In Fig. 13 (c), the transformed prostatic tumor area becomes clear, and the shape and size of the tumor can be observed in the red box. In Fig. 13 (d), it can be observed that the diffusion path of the mammary tumor in the converted PD-weighted sagittal image is more prominent, and more details can be observed around the mammary tumor.

V. CONCLUSION

Traditional MRI can only provide a single disease diagnosis reference due to single contrast in an imaging process. Our PTGAN model based on GAN is the first method to provide two MRI contrasts in an imaging process to the best of our knowledge. Any weighted MRI always contains a small amount other contrasts, which provide a theoretical support for the conversion of T_2-weighted MRI images into PD-weighted MRI images. The research in this paper provides a new imaging method for MRI. A large number of T_2-weighted and PD-weighted images are trained in pairs by PTGAN to map the generated data distribution to real data. The results of various comparative experiments show that our PTGAN model reaches a diagnostic level in brain MRI images and achieves medical observation levels in pathological MRI images.

REFERENCES

[1] M. M. Yallapu, S. F. Othman, E. T. Curtis, B. K. Gupta, M. Jaggi, and S. C. Chauhan, "Multi-functional magnetic nanoparticles for magnetic resonance imaging and cancer therapy," *Biomaterials*, vol. 32, no. 7, pp. 1890–1905, 2011.

[2] P. T. Callaghan, C. D. Eccles, and Y. Xia, "NMR microscopy of dynamic displacements: k-Space and q-space imaging," *J. Phys. E, Sci. Instrum.*, vol. 21, no. 8, p. 820, 1988.

[3] R. Uppaluri, T. Mitsa, M. Sonka, E. A. Hoffman, and G. McLennan, "Quantification of pulmonary emphysema from lung computed tomography images," *Amer. J. Respiratory Crit. Care Med.*, vol. 156, no. 1, pp. 248–254, 1997.

[4] M. Hoehn-berlar, M. Eis, T. Back, K. Kohno, and K. Yamashita, "Changes of relaxation times (T_1, T_2) and apparent diffusion coefficient after permanent middle cerebral artery occlusion in the rat: Temporal evolution, regional extent, and comparison with histology," *Magn. Reson. Med.*, vol. 34, no. 6, pp. 824–834, 1995.

[5] L. G. Nyul, J. K. Udupa, and X. Zhang, "New variants of a method of MRI scale standardization," *IEEE Trans. Med. Imag.*, vol. 19, no. 2, pp. 143–150, Feb. 2000.

[6] W. Liu, Z. Wang, X. Liu, N. Zeng, Y. Liu, and F. E. Alsaadi, "A survey of deep neural network architectures and their applications," *Neurocomputing*, vol. 234, pp. 11–26, Apr. 2017.

[7] M. T. Hagan and M. B. Menhaj, "Training feedforward networks with the Marquardt algorithm," *IEEE Trans. Neural Netw.*, vol. 5, no. 6, pp. 989–993, Nov. 1994.

[8] Q. Le and T. Mikolov, "Distributed representations of sentences and documents," in *Proc. ICML*, Jan. 2014, pp. 1188–1196.

[9] R. Mooney, "Relational learning of pattern-match rules for information extraction," in *Proc. AAAI*, 1999, vol. 334.

[10] A. Krizhevsky, I. Sutskever, and G. E. Hinton, "ImageNet classification with deep convolutional neural networks," in *Proc. NIPS*, 2012, pp. 1097–1105.

[11] A. Graves, A.-R. Mohamed, and G. Hinton, "Speech recognition with deep recurrent neural networks," in *Proc. ICASSP*, May 2013, pp. 6645–6649.

[12] I. Goodfellow *et al.*, "Generative adversarial nets," in *Proc. NIPS*, 2014, pp. 2672–2680.

[13] A. A. Taha and A. Hanbury, "Metrics for evaluating 3D medical image segmentation: Analysis, selection, and tool," *BMC Med. Imag.*, vol. 15, no. 1, p. 29, 2015.

[14] E. Smistad, T. L. Falch, M. Bozorgi, A. C. Elster, and F. Lindseth, "Medical image segmentation on GPUs—A comprehensive review," *Med. Image Anal.*, vol. 20, no. 1, pp. 1–18, 2015.

[15] Y. Bar, I. Diamant, L. Wolf, S. Lieberman, E. Konen, and H. Greenspan, "Chest pathology detection using deep learning with non-medical training," in *Proc. ISBI*, Apr. 2015, pp. 294–297.
[16] N. Tajbakhsh *et al.*, "Convolutional neural networks for medical image analysis: Full training or fine tuning?" *IEEE Trans. Med. Imag.*, vol. 35, no. 5, pp. 1299–1312, May 2016.
[17] Q. Li, W. Cai, X. Wang, Y. Zhou, D. D. Feng, and M. Chen, "Medical image classification with convolutional neural network," in *Proc. ICARCV*, Dec. 2014, pp. 844–848.
[18] A. Kumar, J. Kim, D. Lyndon, M. Fulham, and D. Feng, "An ensemble of fine-tuned convolutional neural networks for medical image classification," *IEEE J. Biomed. Health Inform.*, vol. 21, no. 1, pp. 31–40, Jan. 2017.
[19] F. A. Spanhol, L. S. Oliveira, C. Petitjean, and L. Heutte, "A dataset for breast cancer histopathological image classification," *IEEE Trans. Biomed. Eng.*, vol. 63, no. 7, pp. 1455–1462, Jul. 2016.
[20] C. Leng *et al.*, "Total variation constrained graph regularized NMF for medical image registration," in *Proc. VMSP*, Jul. 2016, pp. 1–5.
[21] F. Yang, M. Ding, X. Zhang, W. Hou, and C. Zhong, "Non-rigid multimodal medical image registration by combining L-BFGS-B with cat swarm optimization," *Inf. Sci.*, vol. 316, pp. 440–456, Sep. 2015.
[22] O. Ronneberger, P. Fischer, and T. Brox, "U-Net: Convolutional networks for biomedical image segmentation," in *Proc. MICCAI*, Oct. 2015, pp. 234–241.
[23] H. Dong, G. Yang, F. Liu, Y. Mo, and Y. Guo, "Automatic brain tumor detection and segmentation using U-Net based fully convolutional networks," in *Proc. MIUA*, Jul. 2017, pp. 506–517.
[24] H. Zhao, O. Gallo, I. Frosio, and J. Kautz, "Loss functions for image restoration with neural networks," *IEEE Trans. Comput. Imag.*, vol. 3, no. 1, pp. 47–57, Mar. 2017.
[25] I. L. Pykett *et al.*, "Principles of nuclear magnetic resonance imaging," *Radiology*, vol. 143, no. 1, pp. 157–168, 1982.
[26] Y. Acremann *et al.*, "Imaging precessional motion of the magnetization vector," *Science*, vol. 290, no. 5491, pp. 492–495, 2000.
[27] L. Axel and L. Dougherty, "MR imaging of motion with spatial modulation of magnetization," *Radiology*, vol. 171, no. 3, pp. 841–845, 1989.
[28] M. A. A. Van Walderveen *et al.*, "Correlating MRI and clinical disease activity in multiple sclerosis relevance of hypointense lesions on short-TR/short-TE ($T_{1-weighted}$) spin-echo images," *Neurology*, vol. 45, no. 9, pp. 1684–1690, 1995.
[29] R. C. Nelson *et al.*, "Focal hepatic lesions: Detection by dynamic and delayed computed tomography versus short TE/TR spin echo and fast field echo magnetic resonance imaging," *Gastrointestinal Radiol.*, vol. 13, no. 1, pp. 115–122, 1988.
[30] R. Deichmann, C. Schwarzbauer, and R. Turner, "Optimisation of the 3D MDEFT sequence for anatomical brain imaging: Technical implications at 1.5 and 3 T," *NeuroImage*, vol. 21, no. 2, pp. 757–767, 2004.
[31] J. B. Fiebach *et al.*, "MRI in acute subarachnoid haemorrhage; findings with a standardised stroke protocol," *Neuroradiology*, vol. 46, no. 1, pp. 44–48, 2004.
[32] P.-F. Van de Moortele, E. J. Auerbach, C. Olman, E. Yacoub, K. Uğurbil, and S. Moeller, "T_1 weighted brain images at 7 Tesla unbiased for proton density, T_2^* contrast and RF coil receive B_1 sensitivity with simultaneous vessel visualization," *NeuroImage*, vol. 46, no. 2, pp. 432–446, 2009.
[33] O. M. Girard *et al.*, "Optimization of iron oxide nanoparticle detection using ultrashort echo time pulse sequences: Comparison of T_1, T_2^*, and synergistic $T_1^* - T_2^*$ contrast mechanisms," *Magn. Reson. Med.*, vol. 65, no. 6, pp. 1649–1660, 2011.
[34] M. Zinkevich, M. Weimer, L. Li, and A. J. Smola, "Parallelized stochastic gradient descent," in *Proc. NIPS*, 2010, pp. 2595–2603.
[35] J. Schulman, F. Wolski, P. Dhariwal, A. Radford, and O. Klimov. (2017). "Proximal policy optimization algorithms." [Online]. Available: https://arxiv.org/abs/1707.06347
[36] D. Needell, R. Ward, and N. Srebro, "Stochastic gradient descent, weighted sampling, and the randomized Kaczmarz algorithm," in *Proc. NIPS*, 2014, pp. 1017–1025.
[37] H. Liu, Z. Wu, X. Li, D. Cai, and T. S. Huang, "Constrained nonnegative matrix factorization for image representation," *IEEE Trans. Pattern Anal. Mach. Intell.*, vol. 34, no. 7, pp. 1299–1311, Jul. 2012.
[38] L. Bai and E. R. Hancock, "Graph kernels from the Jensen-Shannon divergence," *J. Math. Imag. Vis.*, vol. 47, nos. 1–2, pp. 60–69, 2013.
[39] P. N. Rathie, M. Coutinho, T. R. Sousa, G. S. Rodrigues, and T. B. Carrijo, "Stable and generalized-t distributions and applications," *Commun. Nonlinear Sci. Numer. Simul.*, vol. 17, no. 12, pp. 5088–5096, 2012.
[40] X. Mao, Q. Li, H. Xie, R. Y. Lau, Z. Wang, and S. P. Smolley, "Least squares generative adversarial networks," in *Proc. ICCV*, Oct. 2017, pp. 2813–2821.
[41] M. D. Zeiler and R. Fergus. (2013). "Stochastic pooling for regularization of deep convolutional neural networks." [Online]. Available: https://arxiv.org/abs/1301.3557
[42] S. Han, J. Pool, J. Tran, and W. J. Dally, "Learning both weights and connections for efficient neural network," in *Proc. NIPS*, 2015, pp. 1135–1143.
[43] Y. Kim. (Aug. 2014). "Convolutional neural networks for sentence classification." [Online]. Available: https://arxiv.org/abs/1408.5882
[44] J. H. Duyn, Y. Yang, J. A. Frank, and J. W. van der Veen, "Simple correction method for*k*-space trajectory deviations in MRI," *J. Magn. Reson.*, vol. 132, no. 1, pp. 150–153, 1998.
[45] G. Yang *et al.*, "DAGAN: Deep de-aliasing generative adversarial networks for fast compressed sensing MRI reconstruction," *IEEE Trans. Med. Imag.*, vol. 37, no. 6, pp. 1310–1321, Jun. 2018.
[46] H. Dong *et al.*, "TensorLayer: A versatile library for efficient deep learning development," in *Proc. ACMMM*, Oct. 2017, pp. 1201–1204.
[47] D. P. Kingma and J. Ba. (2014). "Adam: A method for stochastic optimization." [Online]. Available: https://arxiv.org/abs/1707.08551
[48] P. Sermanet, S. Chintala, and Y. LeCun, "Convolutional neural networks applied to house numbers digit classification," in *Proc. ICPR*, Nov. 2012, pp. 3288–3291.

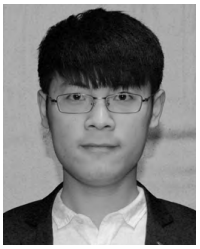

TIAO CHEN is currently pursuing the master's degree with the College of Computer Science and Communication Engineering, Jiangsu University. His research interests include image processing and computer vision under deep learning.

XUEHUA SONG received the B.S. and master's degrees from Shanghai Jiaotong University in 2001 and the Ph.D. degree from Jiangsu University, Jiangsu, China, in 2011. She is currently a Professor with the School of Computer Science and Communication Engineering, Jiangsu University. Her recent research interests focus on digital signal processing.

CHANGDA WANG was a Visiting Researcher with Carleton University and Purdue University. He is currently a Professor with the School of Computer Science and Communication Engineering, Jiangsu University. His recent research interests focus on IoT security, network communication, and cloud computing. He is a member of CCF and serves on the Network and Data Communication Committee. He was a recipient of the Qinglan and Liuda Gaofeng Awards of Jiangsu Province.